

CHANDRA VIEW OF KES 79: A NEARLY ISOTHERMAL SNR WITH RICH SPATIAL STRUCTURE

M. SUN, F. D. SEWARD, R. K. SMITH, P. O. SLANE

Harvard-Smithsonian Center for Astrophysics, 60 Garden St., Cambridge, MA 02138; msun@cfa.harvard.edu

Draft version July 31, 2021

ABSTRACT

A 30 ks *Chandra* ACIS-I observation of Kes 79 reveals rich spatial structures, including many filaments, three partial shells, a loop and a “protrusion”. Most of them have corresponding radio features. Regardless of the different results from two non-equilibrium ionization (NEI) codes, temperatures of different parts of the remnant are all around 0.7 keV, which is surprisingly constant for a remnant with such rich structure. If thermal conduction is responsible for smoothing the temperature gradient, a lower limit on the thermal conductivity of $\sim 1/10$ of the Spitzer value can be derived. Thus, thermal conduction may play an important role in the evolution of at least some SNRs. No spectral signature of the ejecta is found, which suggests the ejecta material has been well mixed with the ambient medium. From the morphology and the spectral properties, we suggest the bright inner shell is a wind-driven shell (WDS) overtaken by the blast wave (the outer shell) and estimate the age of the remnant to be ~ 6 kyr for the assumed dynamics. Projection is also required to explain the complicated morphology of Kes 79.

Subject headings: ISM: supernova remnants: individual (Kes 79) — X-rays: ISM — conduction — stars: winds

1. INTRODUCTION

Kes 79 (G33.6+0.1) is a Galactic SNR with appreciable X-ray and radio structure (Frail & Clifton 1989; Seward & Velusamy 1995). In the radio band, there is an incomplete outer shell from the southwest to the west with a radius of $\sim 6'$ and two prominent indentations in the east and northeast. The radio emission from the center is bright, composed of an “inner ring” and many knots (Frail & Clifton 1989). Strong ^{12}CO J=1 \rightarrow 0 emission and HCO^+ J=1 \rightarrow 0 emission (Scoville et al. 1987; Green & Dewdney 1992) were found at the system velocity of the remnant ($\sim 105 \text{ km s}^{-1}$), located east and southeast of Kes 79. Green & Dewdney (1992) conclude that these imply an interaction of the remnant with adjacent molecular clouds. Frail & Clifton (1989) measured a HI kinematic distance of 10 ± 2 kpc for Kes 79. Case & Bhattacharya (1998) used a new Galactic rotation curve to revise this distance to 7.1 kpc.

ROSAT observations show Kes 79 has strong central shell-like emission and diffuse faint emission extended to the radio outer shell (Seward & Velusamy 1995). Most X-ray emission is from a bright diffuse inner region where there are also bright radio filaments. *ASCA* spectra of Kes 79 show strong Mg, Si, S and Fe-L lines and the global spectrum can be fitted well by a single NEI model (Sun & Wang 2000; Tsunemi & Enoguchi 2002). Kes 79 was listed as a possible mixed-morphology SNR by Rho & Petre (1998) but the unusual double-shell structure (Seward & Velusamy 1995) and X-ray / radio bright structures around the center imply something unique.

We obtained a *Chandra* AO-2 30 ks observation of Kes 79 in 2001. A preceding paper (Seward et al. 2003; S03 hereafter) describes the discovery of a compact central object (CCO) which implies that the remnant has a massive star progenitor. This paper concerns the thermal diffuse emission. The *Chandra* data reduction is described in §2. Spatial features detected in this observation are discussed in §3. §4 describes the X-ray

spectral analysis. §5 is the discussion and §6 is the conclusion. Throughout this paper, we use a distance $d = 7.1$ kpc. Thus, $1' = 2.06$ pc. Dimensions, luminosities, densities, and masses scale as d , d^2 , $d^{-1/2}$, and $d^{5/2}$, respectively.

2. *Chandra* OBSERVATIONS & DATA REDUCTION

The *Chandra* observation is summarized in Table 1. The aimpoint is on the normal position of the I3 CCD. We generally follow the CIAO science threads for the *Chandra* data reduction¹. The data were telemetered in Faint mode and events with *ASCA* grades 1, 5 and 7 were excluded. Known bad columns, hot pixels, and CCD node boundaries also were excluded. After removal of background flares, the effective exposure is 29.3 ks. We applied the CXC correction for charge transfer inefficiency (CTI). The slow gain changes in ACIS CCDs I0-I3 were also corrected using the program ‘corr_tgain’ by A. Vikhlinin². Without this correction, offsets between the observed line centroid and models were observed, which degrade fits significantly. This correction significantly improves fits but has only a small effect on best-fit temperatures (within 5%). An empirical correction to the ACIS low energy quantum efficiency (QE) degradation was performed³. The effective area below 1.8 keV in the front-illuminated CCDs was corrected by a factor of 0.93 to improve the cross-calibration with the back-illuminated CCDs⁴. The response files were produced by CALCRMF and CALCARE.

It is crucial to subtract background properly for the analysis of extended sources. The observed region is located in the Galactic plane. Thus, we have to properly subtract the “Galactic Ridge” emission (e.g., Warwick et al. 1985; Kaneda et al. 1997). We cannot simply subtract the standard ACIS blank sky background⁵ because it is for high Galactic latitude regions. Although parts of the ACIS-I chips are source-free, we cannot simply use the spectrum of those regions as background

¹ <http://cxc.harvard.edu/ciao/threads/index.html>

² <http://cxc.harvard.edu/contrib/alexey/tgain/tgain.html>

³ http://cxc.harvard.edu/cal/Links/Acis/acis/Cal_prods/qeDeg/index.html

⁴ http://asc.harvard.edu/cal/Links/Acis/acis/Cal_prods/qe/12_01_00/

⁵ <http://cxc.harvard.edu/contrib/maxim/bg/index.html>

spectrum because the detector response varies across the CCDs. Therefore, we used a “double subtraction” method to subtract background in the spectral analysis. Similar methods have been applied to clusters (e.g., Markevitch & Vikhlinin 2001). We extracted the spectrum from regions outside of the remnant (excluding point sources). First, we used the high-latitude blank sky background (particle background + Cosmic X-ray background, without “Galactic ridge” emission) to do the first subtraction. The normalization of the blank sky background was scaled up 8% based on the observed count rate in PHA channel 2500 - 3000 ADU. This first subtraction enables the removal of particle background from the spectra. The residual is the vignetted “Galactic Ridge” emission plus over-subtracted CXB because of the high absorption in the direction of Kes 79. Second, we fit the residual with an arbitrary model (power law + some gaussians). The fit is satisfactory with χ^2 of about 1.2. This model was taken as the “background residual model”. For the spectra from each region, we first subtract the blank sky background, and then subtract the residual background with the best-fit model derived above. The normalization of the model is determined by the solid angle of the region of interest. The uncertainty of the background residual model is also included in the uncertainties of the derived properties (e.g., temperature, absorption and abundances).

CIAO 2.2.1, FTOOLS 5.1, XSPEC 11.2 and SPEX 2.0 were used for data analysis. The calibration data used was CALDB 2.23 from the CXC. The uncertainties in this paper are 90% confidence intervals unless specified otherwise.

3. SPATIAL STRUCTURES

The *Chandra* 0.5 - 3 keV exposure-corrected image of Kes 79 is shown in Fig. 1. With the angular resolution of *Chandra*, filaments, multiple shells and loops are revealed. Most of the X-ray emission is from the central region but there is no X-ray enhancement around the central point source. The bright inner shell is fragmented, as are the bright filaments. Just outside the bright inner shell, there are two faint arcs which we name “middle shell”. The arc of this middle shell is short. It only exists in the west and seems to merge with the inner shell in the south. Narrow-band images centered at the Mg, Si and S emission lines were also extracted and do not show appreciable differences from the broadband image.

There are many similarities between the radio and X-ray images. A radio image of Kes 79 is shown in Fig. 2. Fig. 3 shows an adaptively smoothed exposure-corrected X-ray image with radio contours superposed. The faint X-ray outer shell and a northeastern “protrusion” are clearly revealed. The X-ray outer shell well matches the radio outer shell, which is the expected signature of the blast-wave. The X-ray “protrusion” is also coincident with a radio “protrusion”, which is probably a relatively low density region between eastern clouds. The eastern radio limb also matches X-ray filaments. Some of the radio bright clumps around the center (but not all) also match X-ray bright regions. At the X-ray middle shell, there is an excess of radio emission, which may imply compression by shocks so that the particle energy density and magnetic field are amplified. However, we also notice a radio-dim region filled with X-ray bright filaments to the east of the central point source.

The central *Chandra* point source (S03), is close to the geometric center of the remnant in both X-ray and radio (Fig. 2 and

3). However, it is neither at the center defined by the radio/X-ray outer shell, nor the center defined by X-ray bright inner shell and middle shell (Fig. 1 and 2), which is $1' - 1.5'$ to the northeast.

Because the south-west (SW) of the remnant is more radially ordered than other parts, we measured the radial surface brightness profiles in two SW sectors (SW #1 and SW #2, Fig. 4). Three discontinuities (the inner, middle and outer shells) are present in SW #2, while only two (the inner and outer shells) are present in SW #1. Thus, there are three apparent shells in a small portion of the remnant (west to southwest). The surface brightness of the outer shell in the two sectors agrees well. We assume spherical symmetry of the X-ray emission in these two sectors and perform the deprojection to obtain the electron density, a technique broadly applied in galaxy cluster studies (e.g., Fabian et al. 1981). The X-ray gas filling factor is assumed unity. The temperature and abundances in corresponding regions are used to derive the X-ray emissivity. The density of the outer shell is $\sim 0.3 - 0.4 \text{ cm}^{-3}$, while that of the inner shell is $\sim 2 \text{ cm}^{-3}$ (all for a filling factor of unity). Density jumps with factors of 2 - 4 occur across the discontinuities.

4. SPECTRAL ANALYSIS

4.1. The average spectral properties and luminosity

We first want to investigate the average spectral properties of Kes 79 and compare with those derived from previous observations, e.g., *ASCA*. The method of background subtraction was discussed in §2. The global *Chandra* 0.8 - 6 keV spectrum of Kes 79 is shown in Fig. 5. The emission lines from He-like Ne, Mg, Si and S are significant. The Fe-L blend is also significant as a wide bump between the Ne and Mg lines. We first applied collisional ionization equilibrium (CIE) models (e.g., VEQUIL in XSPEC) to fit the spectrum, but the fit is very poor (Table 2). We then applied two NEI codes broadly used now, VNEI (version 1.1) in XSPEC 11.2⁶ and NEI in SPEX 2.0⁷, to model the spectra. The same abundance table (Anders & Grevesse 1989) was used in the two codes. Absorption, temperature, ionization timescale, and abundances of Ne, Mg, Si, S and Fe are free parameters in models, while the abundances of other elements are fixed at their solar values. The fits are much better than the CIE fit (Table 2). The two NEI codes produce somewhat different results (Table 2) but the SPEX code fits the observed spectrum better. The best-fit SPEX NEI model is shown in Fig. 5. The temperature derived from the SPEX model is 15% higher than that from the XSPEC model. The abundances of Mg, Si and Fe from the SPEX model are also significantly higher. The discrepancy can not be removed by setting absorptions to be the same since decreasing the absorption in SPEX fitting will actually increase the best-fit temperature. The different Fe-L atomic data used in the two codes may partially account for the discrepancy (private communication with J. Kaastra). At this stage, this systematic difference should be kept in mind when we try to understand the data. This discrepancy also requires caution to explain the results of NEI fits.

We also re-analyzed the *ASCA* spectrum of Kes 79 using the current calibration files. The B2 mode data from CCD SIS0 and SIS1 were used. Three nearby Galactic plane observations with the same CCD mode were used as background. Source and background spectra were extracted from the same detector

⁶ There is a version 2.0 VNEI routine in XSPEC 11.2, which uses APED to calculate the spectrum. It produces quite similar results as version 1.1.

⁷ <http://www.sron.nl/divisions/hea/spex/version2.0/>

region. The spectra were also fitted by the VEQUIL, VNEI (XSPEC) and NEI (SPEX) models. Results from SIS0 and SIS1 agree so we fit them simultaneously (Table 2). The two NEI codes still produce different results. Our results are consistent with those of other *ASCA* analyses (Sun & Wang 2000 applying SPEX 1.1 on SIS0 data; Tsunemi & Enoguchi 2002 applying XSPEC 11.1 on both GIS and SIS data). *Chandra* results are consistent with *ASCA* results when the same NEI code is applied, except that the *ASCA* abundances of Mg and Si are $\sim 30\%$ higher than *Chandra* values.

The observed flux and the luminosity of Kes 79 are derived from the best-fit of the *Chandra* global spectrum and the total count rate. The two NEI models still produce different results. The derived 0.5 - 10 keV flux (absorbed) is $1.2 - 1.3 \times 10^{-11}$ ergs $\text{s}^{-1} \text{cm}^{-2}$. The 0.5 - 10 keV luminosity is $2.3 - 2.8 \times 10^{36}$ ergs s^{-1} . These values are consistent with those derived from *ASCA*. The CCO only contributes $\sim 0.13\%$ of the total flux.

4.2. The spectral properties of individual regions

We study the spectral variation across the remnant by performing spectral analysis on 14 regions (Fig. 6). All spectra are similar with three strong emission lines. None can be fitted well by CIE models. We also applied the two NEI codes on these spectra. The fits are satisfactory with χ^2_ν ranging from 0.6 to 1.25 (for degrees of freedom from 34 to 107). The derived temperature and absorption distributions are shown in Fig. 6. The temperatures derived from SPEX fits are still systematically higher than those from XSPEC fits, while the absorption from SPEX fits are generally $\sim 10\%$ higher. Regions 7 and 13 have the lowest surface brightness. If we allow both the temperature and the abundances to vary, the uncertainties are big. Thus, for simplicity, we fix the abundances in regions 7 and 13 to the solar values. For other regions with higher surface brightness, we also tried to fit their spectra with solar abundances. In those cases, the fits can be significantly improved if the abundances are allowed to vary.

Regardless of the systematic discrepancy of results from the two codes, there is little temperature variation across the remnant, no matter the geometry and location. This is surprising since there are rich and different gas features in the remnant, which reflects the complexity of the environment. This may give rise to a variation of shock velocity in different regions. Thus a nearly isothermal SNR is not expected.

The measured ionization timescales are model dependent and have large uncertainties, but are all around $10^{11} \text{cm}^{-3} \text{s}^{-1}$. The spectral fits also show some variation of absorption. The absorption in the west and northwest is higher than that in the southeast. If we fix the absorption to the average value, the change of best-fit temperature is at most 10%.

As shown in the global fits (Table 2), the two NEI codes produce different Mg, Si and Fe abundances. A similar discrepancy is observed on fits for individual regions. For the ACIS spectrum with relatively low spectral resolution, the determination of the abundance is not so robust as that of temperature. None of the regions show more than 90% significantly different abundances relative to the average values, including the bright inner shell. This rules out a shocked-ejecta nature of the bright inner shell. The X-ray bright inner shell and clumps are more likely clouds overrun by the shock and are now cooling and evaporating in the hot post-shock region. The failure to find ejecta-dominant regions implies that the SN debris is well-mixed with other material.

5. DISCUSSION

5.1. Thermal conduction

The effect of thermal conduction in the evolution of SNRs is controversial. Conventional wisdom says that thermal conduction is severely suppressed in the disjointed magnetic field, which may be common in SNRs. However, it has been argued that this effect may not be significant in some stages of evolution (e.g., Cox et al. 1999; Kawasaki et al. 2002). Chevalier (1999) also argued that molecular clouds have a significant uniform magnetic field component so that thermal conduction is likely to be important in the hot interior. Cox et al. (1999) proposed a model to explain X-ray thermal-composite SNRs, which depends crucially on efficient thermal conduction to smooth the radial temperature gradient and increase central X-ray brightness. However, there has been little observational evidence for efficient thermal conduction in SNRs. This *Chandra* observation of Kes 79 may provide such evidence.

The nearly uniform temperature distribution of Kes 79 can be used to put a lower limit on thermal conductivity. The scale length of the temperature gradient is $l_T = T_e / |\nabla T_e|$. For any two distinct regions (e.g., 1 and 3 in Fig. 6), l_T should be at least comparable to the separation of two regions (~ 4 pc for regions 1 and 3). The electron free path (λ_e) in Kes 79 is $0.2 (T_e / 0.7 \text{ keV})^2 (n_e / 1 \text{ cm}^{-3})^{-1}$ pc, which is two orders of magnitude smaller than the size of the remnant. Thus, thermal conduction should be classical on the remnant scale. On smaller scales, thermal conduction may be saturated especially at the interface between the hot gas and clouds (e.g., White & Long 1991). Assuming the Spitzer thermal conductivity, the conduction timescale (e.g., Sarazin 1988) is:

$$t_{\text{cond}} \equiv - \left(\frac{d \ln T_e}{dt} \right)^{-1} \approx \frac{\kappa n_e l_T^2}{\kappa} \\ \simeq 38 \left(\frac{n_e}{1 \text{ cm}^{-3}} \right) \left(\frac{l_T}{10 \text{ pc}} \right)^2 \left(\frac{kT_e}{0.7 \text{ keV}} \right)^{-5/2} \left(\frac{\ln \Lambda}{32} \right) \text{ kyr}$$

where κ is the collisional conductivity derived by Spitzer (see the expression for κ in e.g., Sarazin 1988), and $\ln \Lambda$ is the Coulomb logarithm, which is ~ 32 for the typical plasma temperature and density in Kes 79. For the typical electron density in the remnant (1 cm^{-3}) and typical separation of regions in Fig. 6 ($\sim 2'$ or 4.1 pc), the conduction timescale is ~ 6.4 kyr, which is about the age of the remnant (§5.4). Thus, if we attribute the smooth temperature distribution to the effect of thermal conduction, the thermal conductivity should be close to the Spitzer value. Even if heat flux is mainly transported in lower density regions and the uncertainty of the age is considered, the lower limit on the thermal conductivity is $\sim 1/10$ of the Spitzer value.

Both the radio and X-ray morphology of Kes 79 show that it is located in a non-uniform environment and is probably interacting with clouds, which should produce complicated magnetic field structure. Thus, we need to understand why thermal conduction is not significantly suppressed. Narayan & Medvedev (2001) show that thermal conductivity can approach one fifth of the Spitzer value if the magnetized plasma has chaotic magnetic field fluctuations extended over two or more decades in length scales. Numerical work by Chandran & Maron (2003) also shows that thermal conduction is only reduced by a factor of 5-10 relative to the Spitzer value in the static field approximation. Cho et al. (2003) used numerical

methods to study thermal conduction in magnetized turbulent gas and found no suppression. Thus, from theoretical points of view, thermal conductivity on the level of 1/10 of the Spitzer value can be achieved in SNRs.

Kes 79 may not be the only SNR with little temperature variation. *ASCA* observations of G69.7+1.0 (Yoshita et al. 2000), 3C400.2 (Yoshita et al. 2001) and 3C391 (Chen & Slane 2001) also show little temperature variation across the remnants. However, these *ASCA* observations only yield spectral information from 2 - 4 regions (compared to 14 regions used in this work). Moreover, none of them appear to display the rich structure seen in Kes 79. *Chandra* and *XMM-Newton* observations could better constrain the temperature variations in these remnants.

5.2. Multi-shell structure

The *Chandra* image of Kes 79 clearly shows multi-shell structure, as do the radio images, especially at 5 GHz (Fig. 3 of Velusamy et al. 1991). The radio middle shell is at the same azimuth of the X-ray middle shell, but more radially outward. The good correspondence of radio and X-ray implies that these shells are caused by shock compression. As shown in the early analysis, none represents the reverse shock. It is unlikely that the ordered shapes of inner and middle shells are caused by engulfed evaporating cloudlets behind the blast wave. There are at least two possibilities that may cause the multi-shell structure.

The first is projection. Tenorio-Tagle, Bodenheimer & Yorke (1985) made simulations on the interaction of SNRs with molecular clouds. If a SN explodes on the outskirts of a molecular cloud, after the shock reaches the edge of the cloud and breaks out, the shock will speed up in the lower density intercloud medium, while the shock in the cloud is still moving slowly. Thus, in the simplest case, we might see two half shells with different radii, where the radius ratio depends on the initial location of the SN event and the density gradient. If the line of sight is perpendicular to the edge of the cloud, we will see the two shells overlap on the sky creating the appearance of a double shell. The heavy element abundances of the two shells will be determined by the ISM abundance. This can roughly explain the outer and inner shells and their abundances.

An alternative explanation requires the presence of a wind-driven shell (WDS). The compact source found in the center of Kes 79 (S03) implies a massive progenitor. Such massive stars are known to have strong stellar winds during their short lifetimes. Thus, Kes 79 may have begun to evolve inside the stellar wind bubble of its progenitor. The presence of a WDS has a significant effect on the evolution and appearance of an SNR. If the WDS is not very massive, when the SN shock hits the WDS, the whole shell expands while the fast-moving blast wave overtakes it and propagates into the undisturbed ambient medium. At the same time, a reflected shock is expected to form and propagate inwards. This results in multi-shell structure of the remnant, with complicated density, temperature and velocity distributions (Tenorio-Tagle et al. 1990, 1991). Severe distortion of the WDS by cooling and Rayleigh-Taylor instabilities is also revealed in 2-D simulations (Tenorio-Tagle et al. 1991). In this picture, the inner shell of Kes 79 is interpreted as an overtaken WDS, evaporating in the interior of the remnant. The opening of the inner shell at the north may indicate a blow-out of the wind, or could be due to the motion of the progenitor towards the south. The outer shell is the blast wave running in the undisturbed medium. The blast wave should have been de-

celerated when crossing the WDS. The middle shell could be the projected outer shell in another direction where the blast-wave has crossed a locally denser medium. A local reflection shock is another possibility.

In summary, both scenarios can roughly explain the observed properties. We prefer the latter since it is a natural consequence of massive star evolution. Projection is still needed to explain the complicated morphology.

However, neither scenario explains the ionization timescales of the inner shell and the outer shell derived from the NEI fitting. The outer shell and inner shell seem to have similar ionization timescales, implying that the denser inner shell is more recently shocked than the outer shell. Both models require the outer shell to be shocked at a later or comparable time than the inner shell. The current spectral measurement of the faint outer shell still, however, has large uncertainties. Future observations may resolve this puzzle.

5.3. Filaments

At least 7 bright or faint clumpy filaments are found in this observation (Fig. 1). They have a width of 6 - 9 arcsec (0.2 - 0.3 pc), compared to their length of 2 - 3 arcmin (3.1 - 6.2 pc). We measured the surface brightness of the two eastern bright filaments and their surroundings. The filaments are brighter by a factor of 12 - 15, implying an average density difference of ~ 4 . This difference is just as predicted for adiabatic shocks. Thus, these two filaments are probably thin shells viewed edge-on. They may also be part of the shocked WDS. There are several filaments in the interior, however, for which this interpretation is less possible. Filament-like structures are also predicted by numerical simulations of shock-cloud interactions (e.g., Xu & Stone 1995), but in simulations, the cloud is fragmented and filament-like structures are very complicated and chaotic. The filaments in the NE sector of Kes 79 seem to be very ordered. This observation provides a challenge to model the interior structure in middle-aged SNRs.

5.4. Age, density and mass of Kes 79

Accurate estimate of age depends on the understanding of the dynamical evolution of the remnant. The simple Sedov solution and the cloudlet evaporation scenario proposed by White & Long (1991) cannot fit the observed properties. In §5.2, we suggest that the bright inner shell may be the overrun WDS, which complicates the dynamical history of the remnant. As pointed out and discussed by Weaver et al. (1977), the WDS can be considered as a thin shell after the cooling in the WDS is important. Chen et al. (2003) derived a semi-analytic solution for SNRs which evolve crossing a density jump in the surrounding medium, also assuming a thin shell. For Kes 79, since the radius of inner shell is small (~ 6 pc), the remnant should be in the free expansion stage before the blastwave hits the WDS. After the hit, the remnant is in the Sedov phase. Thus, we can apply the solution of Chen et al. (2003) to Kes 79. Using a blastwave temperature (T_S) of 0.6 keV, a density ratio β of 0.1 (see the definition in Chen et al. 2003), radii of $3'$ (6.2 pc) and $6'$ (12.4 pc) for the inner and outer shells respectively, the time after the blastwave hits the WDS is $5.2 (T_S/0.6 \text{ keV})^{-1/2}$ kyr, from equ. 7, 8, 10 and 11 in Chen et al. (2003). This result is not sensitive to the choice of β . If the velocity of the blastwave is 5000 - 10000 km s⁻¹ inside the WDS, the age of the remnant is 5.8 - 6.4 kyr. For T_S in the range of 0.4 - 0.7 keV, the age is 5.4 - 7.5 kyr. Not surprisingly, the derived age is close

to the one derived from the Sedov solution (5.9 - 7.8 kyr for a shock temperature of 0.4 - 0.7 keV; Sedov 1959). A lower limit on the age of the remnant can also be derived from the measured ionization timescale. The ionization timescales derived for individual small regions have large uncertainties, but are all around $10^{11} \text{ cm}^{-3} \text{ s}$. Using an average electron density of $0.5 - 1 \text{ cm}^{-3}$, we set a lower limit on the age of remnant: 3.2 - 6.4 kyr, which is consistent with the estimate from dynamics.

The ambient density (n_0) can also be estimated from the work of Chen et al. (2003), $n_0 = 0.36 E_{51} (T_S/0.6 \text{ keV})^{-1} \text{ cm}^{-3}$ for the assumed shock radius and WDS radius, where E_{51} is the explosion energy in the unit of $10^{51} \text{ ergs s}^{-1}$. This may be only the average value, since the large brightness contrast between the inner shell and outer shell may imply a radial ambient density gradient. If we assume a spherical and uniform distribution of the ambient medium, this density corresponds to a swept-up ISM mass of $99 E_{51} (T_S/0.6 \text{ keV})^{-1} M_\odot$. We also can estimate the average electron density and mass of the X-ray emitting gas from the best-fit emission measure. Since the regions within the inner $3'$ radius and at $3' - 6'$ have large surface brightness contrast, the gas properties are derived separately in the two regions. The different emission measure derived from two NEI codes (Table 2) adds some uncertainty here. The projection from the outer bin to the inner bin is estimated by assuming spherical symmetry. The results are: for the inner $3'$, $\bar{n}_e = 0.8 - 1.2 f_1^{-1/2} \text{ cm}^{-3}$ and $M_X = 28 - 40 f_1^{1/2} M_\odot$, for the region between $3'$ and $6'$, $\bar{n}_e = 0.25 - 0.35 f_2^{-1/2} \text{ cm}^{-3}$ and $M_X = 44 - 62 f_2^{1/2} M_\odot$, where f_1 and f_2 are the filling factors of the hot gas in the inner and outer bins respectively. The inner bin (dominant by bright shells and filaments) and the outer bin (mostly faint diffuse emission) should have different filling factors. But in

any cases, it is clear that all the X-ray emitting gas can be the swept-up ISM.

6. CONCLUSION

The *Chandra* observation of SNR Kes 79 has led to the following conclusions:

1. The *Chandra* image of Kes 79 reveals rich spatial structures: filaments, multiple shells, a loop and a "protrusion", implying a complicated environment around Kes 79. Most of the X-ray structures have corresponding radio structures, implying the importance of shock compression.

2. Three shells are detected in the SW part of the remnant. The inner shell may be an evaporating WDS overrun by the blast wave (the outer shell). The middle shell is perhaps due to projection or a reflection shock. The age of the remnant is estimated to be ~ 6 kyr from the assumed dynamics.

3. We do not find regions with significantly enriched heavy elements, including the bright inner shell. This implies that the ejecta have been mixed well with the surrounding medium given the relative youth of the remnant.

4. Regardless of the systematic discrepancy of results from the two codes, there is little temperature variation across the remnant, no matter the geometry and location. If thermal conduction is responsible for smoothing the temperature gradient, a lower limit of $\sim 1/10$ Spitzer value on the thermal conductivity can be obtained. Thus, thermal conduction may have a significant effect in the evolution of SNRs.

We acknowledge inspiring discussions with Y. Chen. We thank the anonymous referee for prompt and valuable comments. This work was supported by NASA Grant GO1-2067X.

REFERENCES

- Anders, E., & Grevesse N. 1989, *Geochimica et Cosmochimica Acta*, 53, 197
Case, G. L., Bhattacharya, D. 1998, *ApJ*, 504, 761
Chandran, J. L., & Maron, J. L. 2003, *ApJ*, submitted (astro-ph/0303214)
Chen, Y., & Slane, P. O. 2001, *ApJ*, 563, 202
Chen, Y., Zhang, F., Williams, R. M., Wang, Q. D. 2003, *ApJ*, 595, 227
Chevalier, R. A. 1999, *ApJ*, 511, 798
Cho, J., Lazarian, A., Honein, A., Knaepen, B., Kassinosnd, S., & Moin, P. 2003, *ApJ*, 589, L77
Fabian, A. C., Hu, E. M., Cowie, L. L., Grindlay, J. 1981, *ApJ*, 248, 47
Frail, D. A., & Clifton T.R. 1989, *ApJ*, 336, 854
Green, D. A., & Dewdney, P. E. 1992, *MNRAS*, 254, 686
Kaneda, H. et al. 1997, *ApJ*, 491, 638
Kawasaki, M. T. et al. 2002, *ApJ*, 572, 897
Markevitch, M., & Vikhlinin, A. 2001, *ApJ*, 563, 95
Narayan, R., & Medvedev, M. V. 2001, *ApJ*, 562, L129
Rho, J., & Petre, R. 1998, *ApJ*, 503, L167
Sarazin, C. L. 1988, *X-Ray Emission from Clusters of Galaxies* (Cambridge: Cambridge Univ. Press)
Scoville, N. Z. et al. 1987, *ApJS*, 63, 821
Sedov, L. I. 1959, *Similarity and Dimensional Methods in Mechanics* (New York: Academic)
Seward, F. D., & Velusamy, T. 1995, *ApJ*, 439, 715
Seward, F. D., Slane, P., Smith, R., & Sun, M. 2003, *ApJ*, 584, 414 (S03)
Sun, M., & Wang, Z. R. 2000, *Adv. Space Res.* 25, 549
Tenorio-Tagle, G., Bodenheimer, P., & Yorke, H. W. 1985, *A&A*, 145, 70
Tenorio-Tagle, G., Bodenheimer, P., Franco, J., Rozyczka, M. 1990, *MNRAS*, 244, 563
Tenorio-Tagle, G., Rozyczka, M., Franco, J., Bodenheimer, P. 1991, *MNRAS*, 251, 318
Tsunemi, H., & Enoguchi, H. 2002, *PASJ*, 54, 735
Velusamy, T., Becker, R. H., & Seward, F. D. 1991, *AJ*, 102, 676
Warwick, R. S., Turner, M. J. L., Watson, M. G., & Willingdale, R. 1985, *Nature*, 317, 218
Weaver, R., McCray, R., Castor, J., Shapiro, P., Moore, R. 1977, *ApJ*, 218, 377
White, R. L., & Long, K. S. 1991, *ApJ*, 373, 543
Xu, J. & Stone, J. 1995, *ApJ*, 454, 172
Yoshita, K., Miyata, E., Tsunemi, H. 2000, *PASJ*, 52, 867
Yoshita, K., Tsunemi, H., Miyata, E., Mori, K. 2001, *PASJ*, 53, 93

TABLE 1

THE *Chandra* OBSERVATION

Observation ID	1982
Observation mode	ACIS-I, 012378
Data mode	Faint
Date	July 31 - August 1, 2001
Total exposure (ks)	29.95
Effective exposure (ks)	29.27
Counting rate (0.5 - 10 keV) (cts/s)	1.7

TABLE 2

THE FIT TO THE GLOBAL SPECTRUM OF KES 79

	ASCA ^a VEQUIL	ASCA ^b VNEI	ASCA ^c NEI	<i>Chandra</i> ^a VEQUIL	<i>Chandra</i> ^b VNEI	<i>Chandra</i> ^c NEI
N_{H} (10^{22} cm $^{-2}$)	1.70 ± 0.05	$1.63^{+0.06}_{-0.05}$	1.78 ± 0.05	1.58 ± 0.04	$1.54^{+0.05}_{-0.04}$	1.67 ± 0.04
T (keV)	$0.56^{+0.02}_{-0.01}$	$0.66^{+0.03}_{-0.02}$	0.78 ± 0.03	0.57 ± 0.01	0.66 ± 0.02	0.76 ± 0.03
τ (10^{11} cm $^{-3}$ s)	-	$0.90^{+0.30}_{-0.19}$	$0.88^{+0.13}_{-0.11}$	-	$0.78^{+0.24}_{-0.16}$	$0.98^{+0.15}_{-0.13}$
Ne	$1.55^{+0.80}_{-0.58}$	$0.52^{+0.16}_{-0.15}$	$0.59^{+0.32}_{-0.28}$	$0.94^{+0.33}_{-0.28}$	0.42 ± 0.11	0.31 ± 0.17
Mg	$1.64^{+0.38}_{-0.27}$	$0.73^{+0.07}_{-0.06}$	$1.87^{+0.24}_{-0.20}$	$1.31^{+0.18}_{-0.15}$	0.60 ± 0.04	$1.46^{+0.14}_{-0.12}$
Si	$1.50^{+0.29}_{-0.22}$	$0.79^{+0.07}_{-0.06}$	$1.33^{+0.14}_{-0.13}$	$1.03^{+0.11}_{-0.10}$	0.57 ± 0.04	$1.01^{+0.09}_{-0.08}$
S	$2.04^{+0.41}_{-0.32}$	$1.08^{+0.15}_{-0.14}$	$1.25^{+0.17}_{-0.15}$	$1.78^{+0.21}_{-0.20}$	$1.04^{+0.15}_{-0.12}$	$1.03^{+0.12}_{-0.11}$
Fe	$1.41^{+0.35}_{-0.25}$	$0.59^{+0.09}_{-0.09}$	$1.92^{+0.35}_{-0.31}$	$1.09^{+0.17}_{-0.15}$	0.48 ± 0.06	$1.52^{+0.22}_{-0.20}$
Norm ^d	5.16 ± 0.74	$6.29^{+0.70}_{-0.65}$	$2.94^{+0.31}_{-0.29}$	5.02 ± 0.42	$5.95^{+0.67}_{-0.49}$	$3.02^{+0.24}_{-0.23}$
χ^2/dof	396.2/182	236.9/181	210.0/175	480.1/163	296.9/162	181.9/136

^a Ionization equilibrium collisional plasma model in XSPEC 11.2

^b Non-equilibrium ionization collisional plasma model (version 1.1) in XSPEC 11.2

^c Non-equilibrium ionization collisional plasma model in SPEX 2.0

^d Normalization of the model ($n_e n_{\text{H}} V$) in units of 10^{58} cm $^{-3}$. We used a distance of 7.1 kpc. Note these values are $\sim 30\%$ less than those of the whole remnant. The big difference in the normalization between XSPEC and SPEX results comes from their difference on modeling the line emission and continuum.

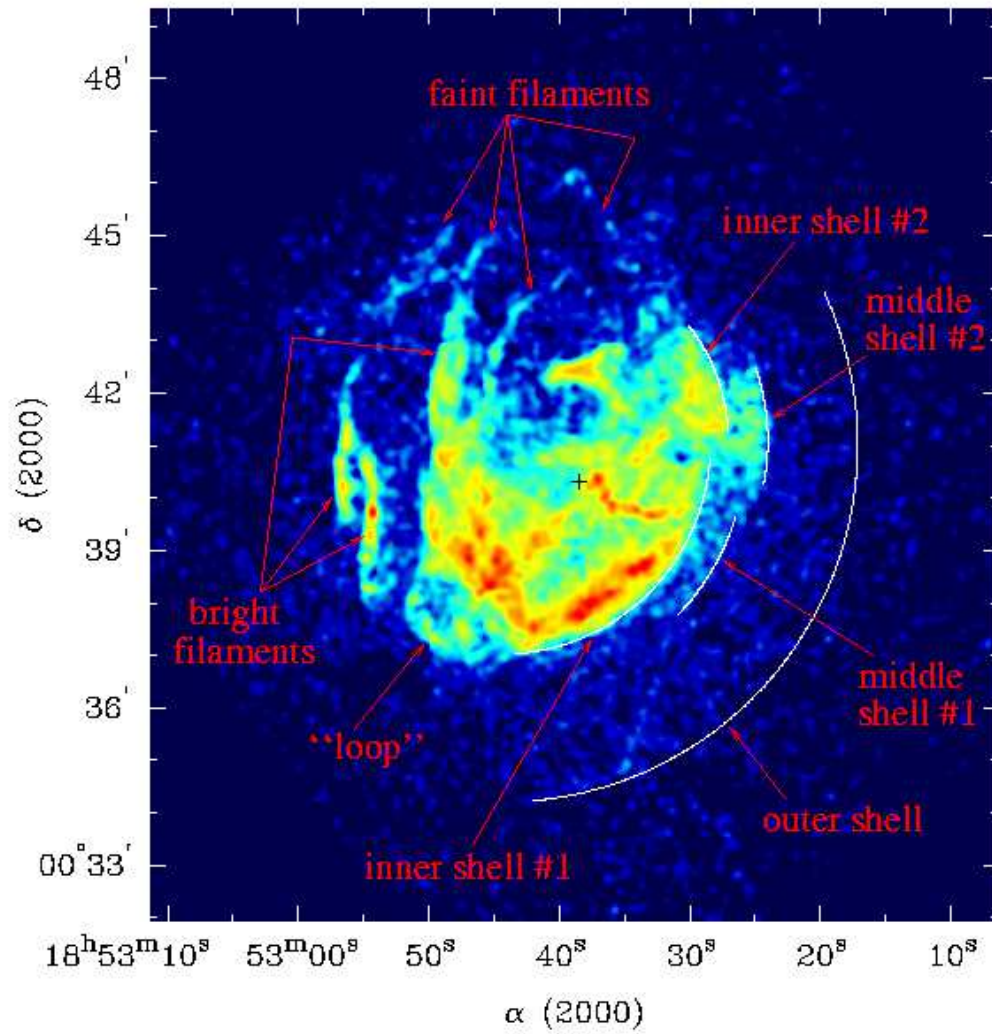


FIG. 1.— The 0.5 - 3 keV *Chandra* image of Kes 79 (exposure-corrected), smoothed by a Gaussian with σ of $4''$. Point sources were removed. Interesting features, including partial shells and filaments, are marked. The black cross shows the position of the central point source (S03).

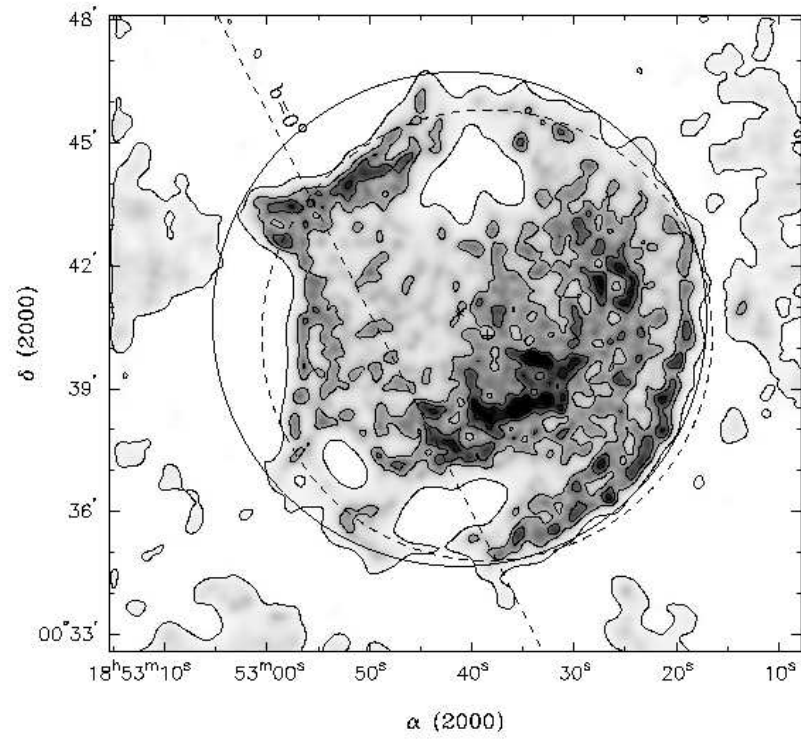


FIG. 2.— VLA 20 cm map of Kes 79 (Velusamy, Becker & Seward 1991) superposed on its own contours. The position of the central X-ray point source is shown by a cross. The large dashed circle is centered at the central point source with a radius of $5.5'$. The curvature of the radio outer shell does not match a circle centered at the point source. The large solid circle (with a radius of $6'$) matches the radio boundary in the N, E, and S well. Its center is marked by an asterisk. The two centers are $\sim 1'$ apart.

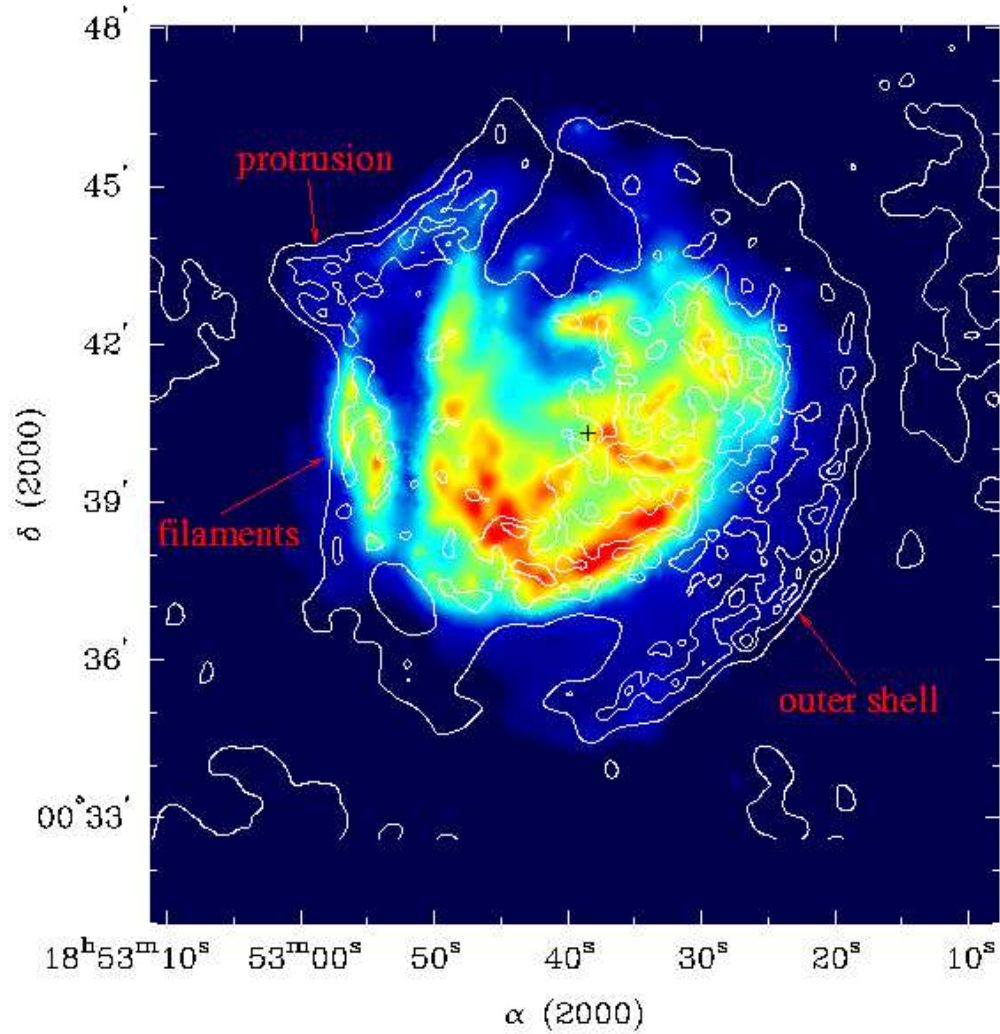


FIG. 3.— *Chandra* image in the 0.5 - 3 keV band (exposure-corrected, adaptively smoothed, shown in square-root scale), superposed on VLA 20 cm contours. The smoothing scale ranges from $6''$ to $20''$ depending on the observed photon statistics. The X-ray outer shell and “protrusion” are better shown in this figure than in Fig. 1. X-ray and radio structures are generally coincident with each other, e.g., the outer shell, part of the bright inner shell, some filaments and the “protrusion”. However, there is a radio-dim, X-ray bright region in the east interior to the radio boundary which is apparently part of the inner ring. The black cross shows the position of the central point source.

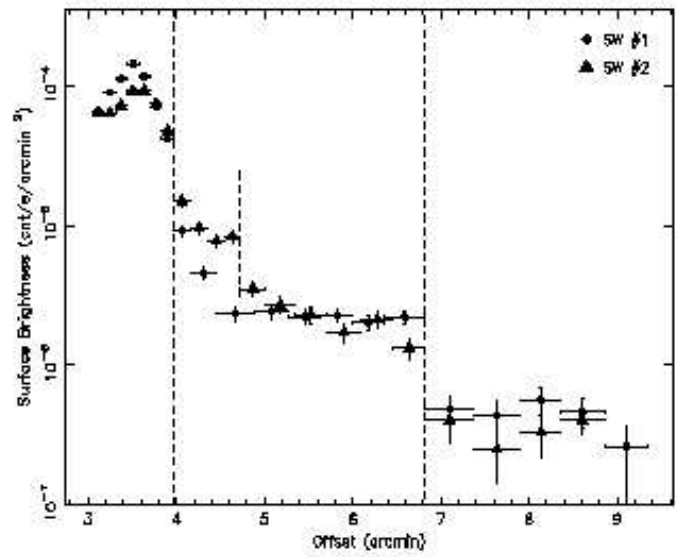
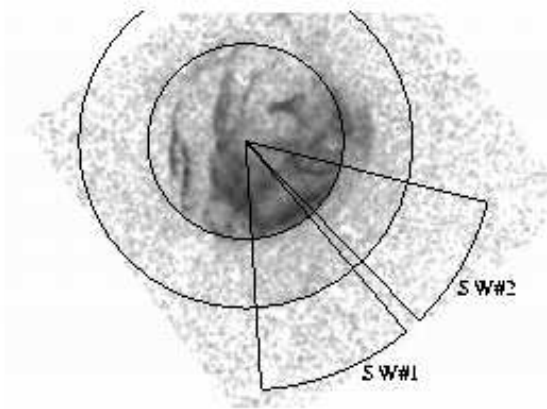


FIG. 4.— The radial surface brightness profiles of two SW sectors. Both sectors have two common surface brightness discontinuities (the inner shell and the outer shell), while SW#2 has an additional discontinuity, the middle shell indicated on the right.

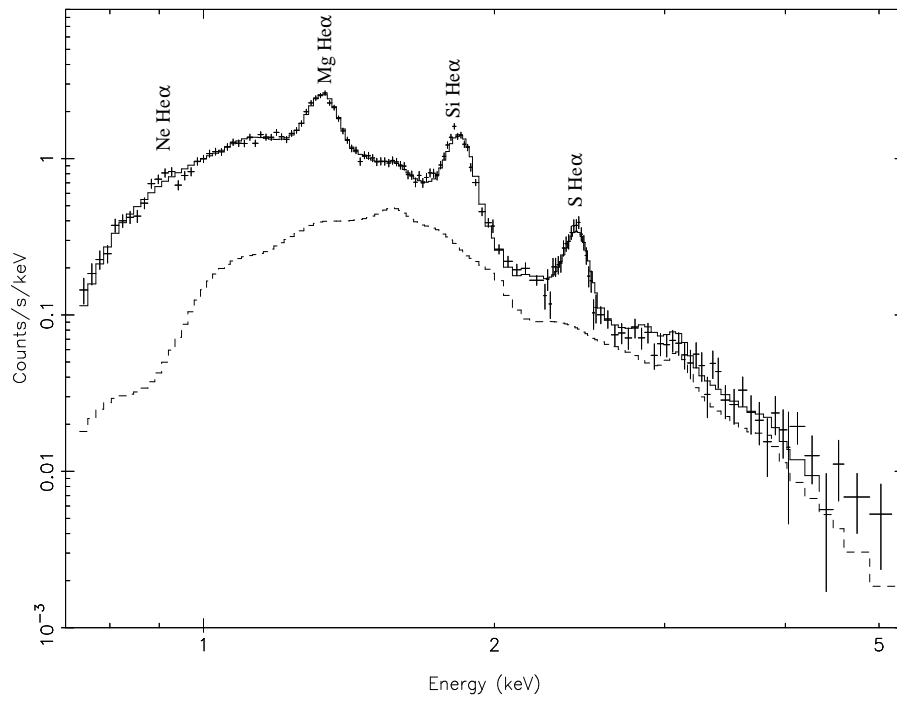


FIG. 5.— The integrated *Chandra* spectrum of the whole remnant with the best-fit NEI model (SPEX 2.0). Emission lines from Ne, Mg, Si and S are labeled. Fe L-blend is also visible between Ne and Mg lines. The dashed line represents the residual emission without the contribution from Ne, Mg, Si, S and Fe.

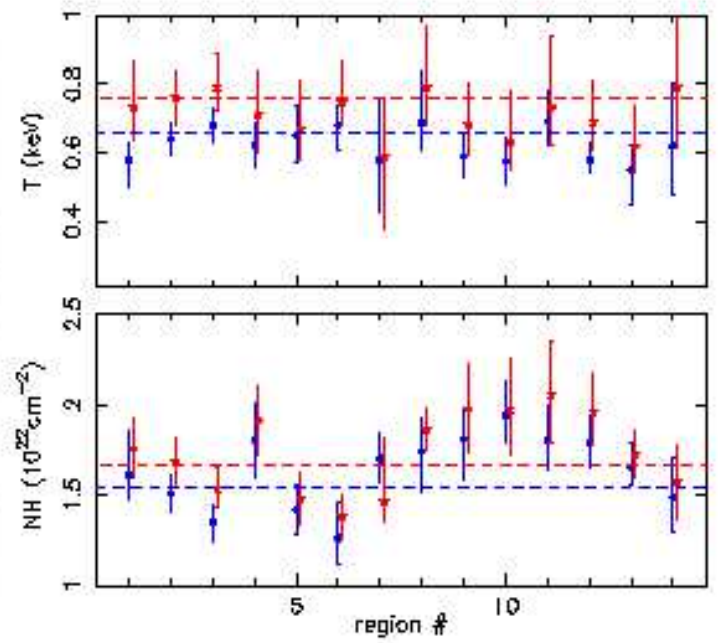
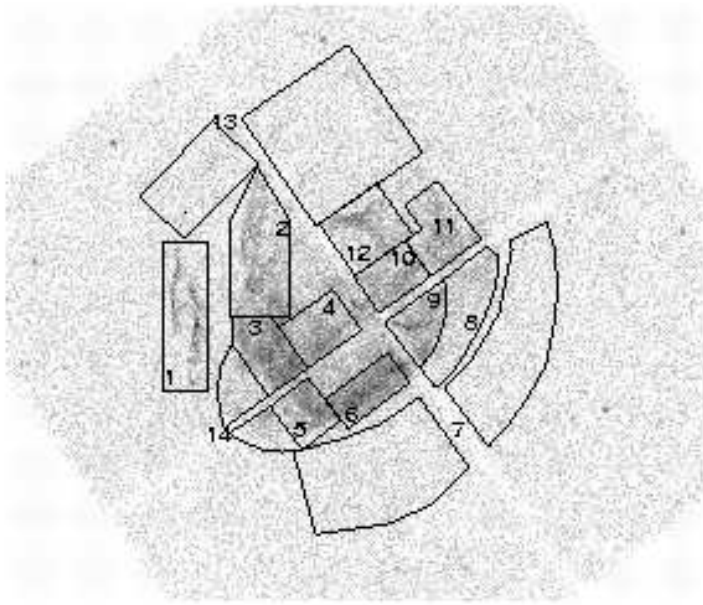


FIG. 6.— The measured temperatures and absorption in 14 regions of Kes 79. The blue points are the results of XSPEC VNEI fits, while the red points are the results of SPEX NEI fits. The dashed lines represent the best fits to the *Chandra* global spectrum. Regardless of the different results from two NEI codes, the temperature variation across the remnant is small, which implies a nearly isothermal state of plasma in Kes 79. The Northwest part of the remnant has higher absorption than the Southeast part.